Circular quantum dots in twisted bilayer graphene

M. Mirzakhani [1,*] F. M. Peeters [2,†] and M. Zarenia [3,‡]

[1]*School of Physics, University of the Witwatersrand, Johannesburg, Wits 2050, South Africa*
[2]*Department of Physics, University of Antwerp, Groenenborgerlaan 171, B-2020 Antwerp, Belgium*
[3]*Department of Physics and Astronomy, University of Missouri, Columbia, Missouri 65211, USA*

Within a tight-binding approach, we investigate the effect of twisting angle on the energy levels of circular bilayer graphene (BLG) quantum dots (QDs) in both the absence and presence of a perpendicular magnetic field. The QDs are defined by an *infinite-mass potential*, so that the specific edge effects are not present. In the absence of magnetic field (or when the magnetic length is larger than the moiré length), we show that the low-energy states in twisted BLG QDs are completely affected by the formation of moiré patterns, with a strong localization at AA-stacked regions. When magnetic field increases, the energy gap of an untwisted BLG QD closes with the *edge* states, localized at the boundaries between the AA- and AB-stacked spots in a twisted BLG QD. Our observation of the spatial localization of the electrons in twisted BLG QDs can be experimentally probed by low-bias scanning tunneling microscopy measurements.

I. INTRODUCTION

Over the past year, twisted bilayer graphene (tBLG), i.e., BLG with relative twist between its two coupled graphene layers, has been the subject of intensive theoretical and experimental research works. The main interest results from the new discovery of superconductivity and correlated insulating phases in tBLG at a so-called *magic* twist angle [1–3]. It is fascinating that with a small twist angle between the two layers of BLG, the electronic and transport properties of the system undergo profound changes. In this paper, we aim to investigate the effect of twisting angle on the energy levels of a circular quantum dot (QD) in tBLG. QDs have been studied extensively in different two-dimensional (2D) materials, i.e., monolayer, bilayer, and few-layer graphene [4–20], transition-metal dichalcogenides [21–23], hexagonal boron nitride [24,25], phosphorene [26,27], etc.

Among QDs in 2D materials, graphene-based QDs (geometry- or gate-induced) with desirable properties for applications have received particular interest [4–20,28–44]. The studies show that the electronic and optical properties of graphene QDs can be tuned by size, shape, edge type, and electrostatic gating; see, e.g., Refs. [4,5,10,16,20,33–35,39,42,43]. Interesting properties, such as the gap opening [11,33,34,43], the appearance of degenerate zero-energy edge states [4,10], magnetic and ferromagnetic ordering [10,29], long-spin relaxation time [10], and realization of tunable multidot systems [44], have been reported in these studies.

The electronic properties of untwisted AB- or AA-stacked BLG QDs have been studied both theoretically

[11,16,38,41,42] and experimentally [15,17]. In a tBLG QD, the twist angle can be used as a new knob to tune the electronic properties of the system. The energy levels and optical properties of small tBLG flakes were recently studied in Ref. [45] at zero magnetic field. In this study, the obtained energy levels are highly influenced by the edge effects of the flakes. The electronic [46–48] and transport [49,50] properties of tBLG nanoribbons have also been investigated, in which the transport properties of the low-energy regime were determined by the interplay between the moiré pattern and the tBLG edges [49]. Another study was devoted to the investigation of the electronic properties of tBLG flakes with irregular shapes [51]. It was shown that the presence of one complete moiré spot in a tBLG flake is sufficient to reproduce the density of states of the corresponding tBLG sheet.

The purpose of this paper is to investigate the effect of twisting angle on the energy levels of circular tBLG QDs, which are completely distinct structures from the AB- or AA-stacked BLG QDs (Fig. 2). To eliminate the effect of edges, we define a circular tBLG QD surrounded by a staggered site-dependent infinite-mass (IM) potential M_0 [Fig. 2(a)]. The mass potential on the layers can be experimentally induced by sandwiching the tBLG sheet between the top and bottom substrates such that the A and B sublattices in each graphene sheet feel a different potential [52].

Using the tight-binding model (TBM), we obtain the energy spectra of tBLG QDs in both the absence and presence of an external magnetic field, and we demonstrate the effect of twisting on the energy levels. In Sec. II we briefly recapitulate the geometry of a tBLG lattice. The proposed QD structure in tBLG, and the basics of our numerical method, are presented in Sec. III. In Secs. IV and V, we present our results for the energy levels and confined states in the absence and presence of a perpendicular magnetic field, respectively. A summary and concluding remarks follow in Sec. VI.

*mohamad.mirzakhani@gmail.com
†francois.peeters@uantwerpen.be
‡zareniam@missouri.edu
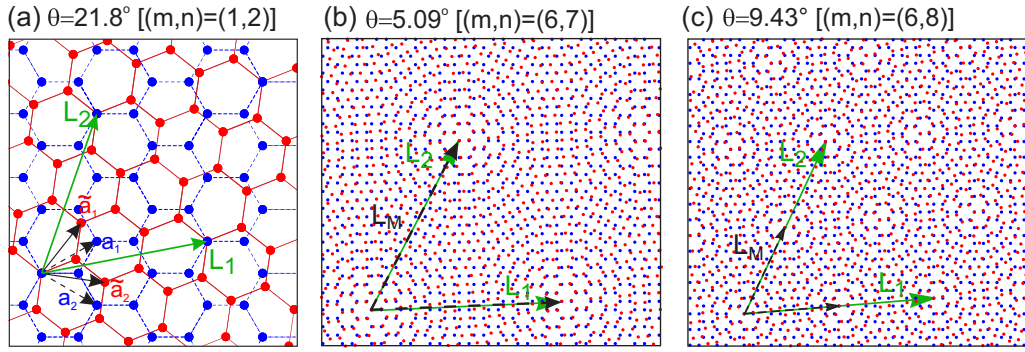
FIG. 1. Crystal structure of the tBLG with (a) $\theta_{1,2} = 21.8°$, (b) $\theta_{6,7} = 5.09°$, and (c) $\theta_{6,8} = 9.43°$. Layers 1 ($A1$, $B1$) and 2 ($A2$, $B2$), respectively, are represented by blue and red circles. The primitive lattice vectors of two layers are denoted by a_i and $\tilde{a}_i$ ($i = 1, 2$). The vectors $\mathbf{L}_1$ and $\mathbf{L}_2$ indicate the lattice vectors of periodic commensurate structure. The moiré superlattice period L_M is shown with the dashed black vectors in (b) and (c) panels.

II. ATOMIC STRUCTURE OF TWISTED BILAYER GRAPHENE

In this section, we briefly review the atomic structure of tBLG. One can find a more detailed and comprehensive study of the tBLG system in Refs. [53–56]. Monolayer graphene (MLG) is a 2D honeycomb lattice of carbon atoms, whose unit cell contains two inequivalent sublattices, A and B. Twisted BLG consists of two graphene layers that are twisted with respect to each other by an angle θ. We define the honeycomb lattice of graphene with the lattice vectors $\mathbf{a}_1 = a(\sqrt{3}/2, 1/2)$ and $\mathbf{a}_2 = a(\sqrt{3}/2, -1/2)$, where $a \approx 0.246$ nm is the lattice constant. In the lower layer (named layer 1), containing $A1$ and $B1$ sublattices, the lattice positions are given by

$$
\begin{aligned}
\mathbf{r}_{A1} &= m\mathbf{a}_1 + n\mathbf{a}_2, \\
\mathbf{r}_{B1} &= m\mathbf{a}_1 + n\mathbf{a}_2 + \delta_1, \qquad (m, n) \in \mathbb{Z},
\end{aligned}
\tag{1}
$$

where $\delta_1 = (\mathbf{a}_1 + \mathbf{a}_2)/3$ connects the nearest-neighbor site inside the unit cell of the graphene lattice.

Here, we define the case of $\theta = 0$ as a perfect AA-stacked BLG, in which each carbon atom in the second layer (with $A2$ and $B2$ sublattices) is vertically displaced by $d_0 = 0.335$ nm (interlayer spacing) from the corresponding atoms in the first graphene sheet. In tBLG, the top graphene layer is rotated with respect to the lower layer by an angle θ around a common site, e.g., the $A1$-$A2$ position [Fig. 1(a)]. Accordingly, the primitive lattice vectors of the rotated layer are given by $\tilde{\mathbf{a}}_i = \mathcal{R}(\theta)\mathbf{a}_i$ ($i = 1, 2$), and thus its atom positions are

$$
\begin{aligned}
\mathbf{r}_{A2} &= m\tilde{\mathbf{a}}_1 + n\tilde{\mathbf{a}}_2, + d_0\mathbf{e}_z, \\
\mathbf{r}_{B2} &= m\tilde{\mathbf{a}}_1 + n\tilde{\mathbf{a}}_2 + d_0\mathbf{e}_z + \tilde{\delta}_1,
\end{aligned}
\tag{2}
$$

where $\mathcal{R}(\theta)$ is a 2 × 2 rotation matrix, $\mathbf{e}_z$ is the unit vector parallel to the z axis, and $\tilde{\delta}_1 = (\tilde{\mathbf{a}}_1 + \tilde{\mathbf{a}}_2)/3$.

In general, the lattice structure of tBLG is not periodic for any θ (incommensurate structure). However, in certain integers m and n, it is possible that the lattice vector of layer 1, $n\mathbf{a}_1 + m\mathbf{a}_2$, coincides with the lattice vector of layer 2, $m\tilde{\mathbf{a}}_1 + n\tilde{\mathbf{a}}_2$, and the structure becomes periodic (commensurate structure). The superlattice structure is thus defined by

the lattice vectors [57]

$$
\begin{aligned}
\mathbf{L}_1 &= n\mathbf{a}_1 + m\mathbf{a}_2 = m\tilde{\mathbf{a}}_1 + n\tilde{\mathbf{a}}_2, \\
\mathbf{L}_2 &= \mathcal{R}(\pi/3)\mathbf{L}_1.
\end{aligned}
\tag{3}
$$

A commensurate twist angle with a periodic *moiré* pattern is given by

$$
\cos(\theta_{m,n}) = \frac{1}{2} \frac{m^2 + n^2 + 4mn}{m^2 + n^2 + mn},
\tag{4}
$$

and the lattice constant of the (commensurate) superlattice $L_{m,n} = |\mathbf{L}_1| = |\mathbf{L}_2|$ is

$$
L_{m,n} = a\sqrt{m^2 + n^2 + mn} = \frac{|m - n|a}{2\sin(\theta/2)}.
\tag{5}
$$

The label (m, n) is used as a representative of a corresponding commensurate twist angle given by Eq. (4).

For twist angles $\theta \lesssim 15°$ [58], due to the mismatch between the lattice vectors of the two layers, the moiré superlattice period $L_M = a/2\sin(\theta/2)$ can be defined for any commensurate or incommensurate θ [55]. Notice that $L_{m,n} = |m - n|L_M$. Obviously, the lattice constant of commensurate superstructure $L_{m,n}$ coincides with the moiré superlattice period L_M when $|m - n| = 1$. Figures 1(b) and 1(c) illustrate the atomic structure of tBLG when $\theta_{6,7} = 5.09°$ ($L_{6,7} = L_M$, $|m - n| = 1$) and $\theta_{6,8} = 9.43°$ ($L_{6,8} = 2L_M$, $|m - n| = 2$), respectively. The electronic properties of tBLG depend on these two lengths scales, $L_{m,n}$ and L_M [58,59].

III. INFINITE-MASS DEFINED CIRCULAR QUANTUM DOTS IN TWISTED BILAYER GRAPHENE

As illustrated in Fig. 2, the QD is built from the two perfectly flat MLG QDs with the same shape, size, and edge boundaries in which the second MLG QD (top) is rotated by an angle θ around the geometry center of the dot. When $\theta = 0$, the system is a perfect AA-stacked BLG QD. The interlayer spacing is d_0.

We consider a circular tBLG dot region with radius R, surrounded by a site-dependent staggered potential with $M_0 = 2.0$ eV [Fig. 2(a)], such that the atoms belonging to the sublattices $A1$ ($A2$) and $B1$ ($B2$) have a mass-term potential of $+M_0$

Layer 1   A1 +M₀
          B1 −M₀

Layer 2   A2 −M₀
          B2 +M₀
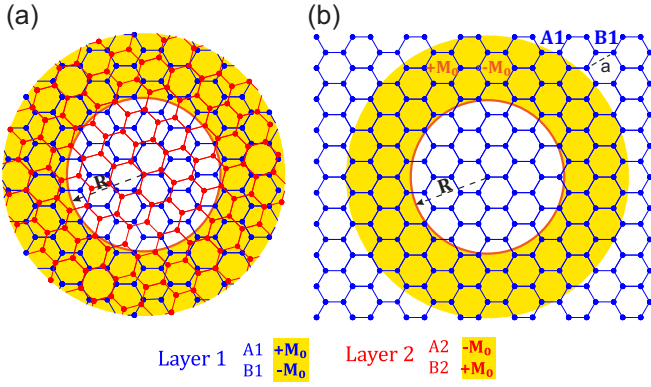
FIG. 2. (a) Schematic geometry of the circular tBLG dot of radius R defined by infinite-mass potential boundary. The atoms of the two layers are represented by blue (layer 1) and red (layer 2) circles. The dot can be considered as two layers of a circular MLG dot (b), where the layers are stacked rotationally. The dot region is surrounded by a site-dependent staggered potential (yellow region), where the atoms belonging to the sublattices $A1$ ($A2$) and $B1$ ($B2$) have mass-term potentials of $+M_0$ ($-M_0$) and $-M_0$ ($+M_0$), respectively.

$(-M_0)$ and $-M_0$ $(+M_0)$, respectively. The staggered potential eliminates the specific edge effects, e.g., the appearance of the zero-mode states due to the zigzag edges.

We use a single-orbital TBM for p_z atomic orbital of carbon, as introduced by Wallace [60]. The TBM Hamiltonian in a second quantization formalism can be written as

$$\mathcal{H} = \sum_i (\epsilon_i + M_i) c_i^\dagger c_i - \sum_{\langle i,j \rangle} t(\mathbf{d}_{ij}) c_i^\dagger c_j + \text{H.c.}, \qquad (6)$$

where $c_i^\dagger$ and c_i are, respectively, the creation and annihilation operators for an electron on the lattice site i with on-site energy ϵ_i and mass-term potential M_i. In the second term, $\mathbf{d}_{ij} = \mathbf{R}_i - \mathbf{R}_j$ is the distance between the lattice points ($\mathbf{R}_i$, $\mathbf{R}_j$), $t(\mathbf{d}_{ij})$ is the corresponding transfer integral, and $\langle i,j \rangle$ indicates a summation over nearest-neighbor sites. In terms of the Slater-Koster form, the transfer integral between the atoms i and j can be written as [55,61–65]

$$-t(\mathbf{d}_{ij}) = V_{pp\pi} \left[1 - \left(\frac{\mathbf{d}_{ij} \cdot \mathbf{e}_z}{d_{ij}} \right)^2 \right] + V_{pp\sigma} \left(\frac{\mathbf{d}_{ij} \cdot \mathbf{e}_z}{d_{ij}} \right)^2,$$

$$V_{pp\pi} = V_{pp\pi}^0 \exp\left(-\frac{d_{ij} - a_{\text{cc}}}{\delta_0} \right)^2, \qquad (7)$$

$$V_{pp\sigma} = V_{pp\sigma}^0 \exp\left(-\frac{d_{ij} - d_0}{\delta_0} \right)^2,$$

where $a_{\text{cc}} = a/\sqrt{3} \approx 0.142$ nm is the carbon-carbon distance of graphene and $\delta_0 = 0.184a$ is the decay length. $V_{pp\pi}^0 \approx -2.7$ eV and $V_{pp\sigma}^0 \approx 0.48$ eV are the intralayer and interlayer nearest-neighbor hopping parameters, respectively. For the intralayer coupling, we include only the nearest-neighbor hopping parameter. But for the interlayer coupling, since the layers are rotated and the neighbors are not on top of each other, we take the interlayer coupling terms for atomic distances of $d_{ij} \leqslant 4a_{\text{cc}}$ [55]. As a result of mixing between the two sublattices, the electron-hole (e-h) symmetry is broken.

In the presence of a magnetic field, the transfer energy becomes $t(\mathbf{d}_{ij}) \rightarrow t(\mathbf{d}_{ij}) e^{i 2\pi \Phi_{ij}}$, where

$$\Phi_{ij} = \frac{1}{\Phi_0} \int_{\mathbf{R}_i}^{\mathbf{R}_j} \mathbf{A}(\mathbf{r}) \cdot d\mathbf{r} \qquad (8)$$

is the Peierls phase [66], with $\Phi_0 = h/e$ the magnetic flux quantum and $\mathbf{A}(\mathbf{r})$ the vector potential. The vector potential corresponding to the external magnetic field $\mathbf{B} = B\mathbf{e}_z$ perpendicular to the tBLG flakes is chosen in the Landau gauge $\mathbf{A} = (0, Bx, 0)$ for which one finds that Φ_{ij} is only nonzero in the y-direction and is given by $\Phi_{ij} = \text{sgn}(y_j - y_i) \frac{(x_j + x_i)}{2\sqrt{3}a} \frac{\Phi}{\Phi_0}$, where $\Phi = \sqrt{3}a^2 B/2$ is the magnetic flux threading one carbon hexagon (a is the graphene lattice constant).

We also calculate the electron and hole current from site j into site i using [50,51,67]

$$I_{ji} = \frac{2e}{\hbar} \text{Im} \sum_{\gamma \gamma'} \mathcal{H}_{i\gamma, j\gamma'} \phi_{j\gamma} \phi_{i\gamma'}^*, \qquad (9)$$

where $\mathcal{H}_{i\gamma, j\gamma'}$ are the TB Hamiltonian matrix elements, $\{\phi_{i\gamma}\}$ are the quantum states on the lattice sites, and γ is the orbital index. The total current at each site i can be obtained using

$$I_i = \sum_j I_{ji} \hat{\mathbf{r}}_{ij}, \qquad (10)$$

where $\hat{\mathbf{r}}_{ij}$ is the unit vector pointing from site i to site j.

IV. ENERGY LEVELS: ZERO MAGNETIC FIELD

In the absence of any external magnetic field, we first consider the energy spectrum of a circular tBLG QD as a function of the twist angle θ at a fixed radius R. Figure 3(a) shows the results for $R = 4.81$ nm. Due to the mass-potential confinement, the QDs exhibit an energy gap between the electron and hole states irrespective of the twist angle. For $10° \lesssim \theta \lesssim 50°$ the interlayer hoppings are weak, the two layers become effectively decoupled, and thus the energy levels
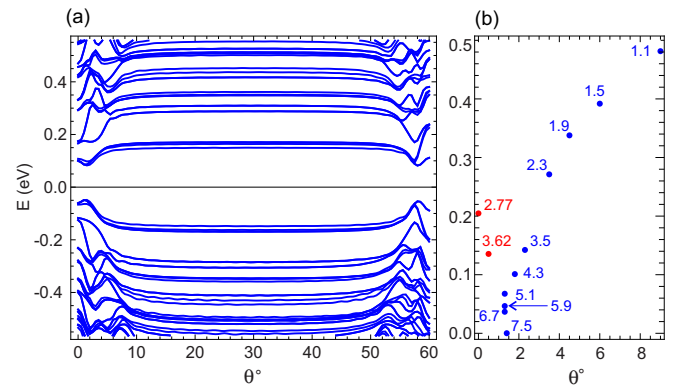
FIG. 3. (a) Energy levels of a circular tBLG QD, of radius $R = 4.81$ nm, as a function of twist angle θ. The angles $\theta = 0°$ and $60°$, respectively, correspond to the AA- and AB-stacked BLG QDs. (b) The minimum-energy states of the first lowest-electron energy (at $\theta < 10°$) for different dot radii. Each case is marked by the corresponding dot radius R. The red-marked points correspond to the dots with the radius of $R = L_{m,n}$ ($R = 2.77$ nm $\approx L_{6,7}$, $R = 3.62$ nm $\approx L_{8,9}$).
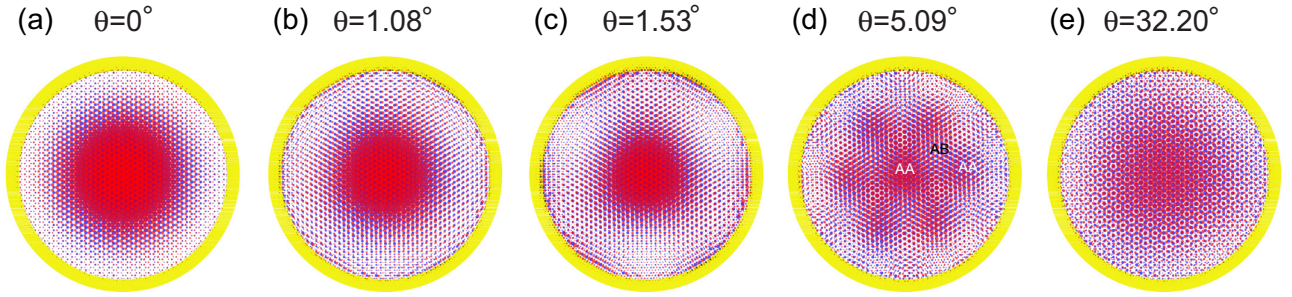
FIG. 4. Probability densities corresponding to the four lowest-electron-energy levels shown in the energy spectrum of Fig. 3 with $R = 4.81$ nm. The results are presented for five different twisting angles (a) $\theta = 0°$ (AA stacking), (b) $\theta = 1.08°$ (magic angle), (c) $\theta = 1.53°$, (d) $\theta_{6,7} = 5.09°$, and (e) $\theta_{1,3} = 32.20°$. Layer 1 (2) is represented by the blue (red) color, and the yellow region indicates the mass potential barrier.

are nearly independent of θ at this range. At $\theta = 0°$ and $60°$, the tBLG structure turns into a prefect AA- and AB-stacked BLG QD, respectively (see the corresponding energy spectra in Refs. [39,42]). At $\theta \lesssim 10°$ and $\theta \gtrsim 50°$, the formation of moiré patterns with well-defined AA and AB-stacked spots (see Fig. 1) modifies the spectrum, and a minimum energy gap appears at $\theta \approx 1.53°$ and $\theta \approx 58.2°$. Figure 3(b) shows the minimum energies of the first lowest-electron state (at $\theta < 10°$) for different QD sizes (labels indicate the corresponding dot radius $R = 1.1$–7.5 nm). We observe that the minimum energy occurs at smaller angles when the dot radius increases. When $R \approx L_{m,n}$, the minimum energy appears at $\theta < 1°$ [see the red points in Fig. 3(b) for $R = 2.77$ nm $\approx L_{6,7}$ and $R = 3.62$ nm $\approx L_{8,9}$].

To better understand this, we define the spatial distribution of the probability densities corresponding to the N lowest-electron-energy states as

$$\rho_{\ell,N} = \sum_{\epsilon_i \in N} \left| \psi_{\epsilon_i}^{\ell}(\mathbf{r}) \right|^2, \tag{11}$$

where $\psi_{\epsilon_i}^{\ell}(\mathbf{r}) = [\phi_{\epsilon_i}^{A\ell}(\mathbf{r}_s), \phi_{\epsilon_i}^{B\ell}(\mathbf{r}_{s'})]^T$ denotes the quantum state of the two layers ($\ell = 1, 2$) with energy ϵ_i. The components $\phi^{A\ell}(\mathbf{r}_s)$ ($s = 1, 2, \ldots, N_{A\ell}$) and $\phi^{B\ell}(\mathbf{r}_{s'})$ ($s' = 1, 2, \ldots, N_{B\ell}$) correspond to the different sublattices $A\ell$ and $B\ell$ in each layer, respectively.

In Figs. 4(a)–4(e), we show $\rho_{\ell,N}$ for the four lowest-energy states ($N = 4$) shown in the spectrum of Fig. 3 at different twist angles (as labeled). In the case of $\theta = 0$ (AA-stacked BLG QD), the lowest-energy state is fourfold degenerate (two for layer and two for valley degeneracy), for which the electrons are equally distributed in both layers [Fig. 4(a)]. As θ increases, the moiré lengths becomes smaller, and well-defined AA- and AB-stacked regions start to form in the QD area. At $\theta = 1.53°$ (the angle at which the minimum energy of the lowest-electron energy occurs), the centrally confined AA-stacked region, which is induced by the mass potential, hybridizes with the moiré-pattern-induced AA-stacked confined regions at the edge of the QD [Fig. 4(c)]. This decreases the energy gap slightly. As θ increases (moiré length decreases), the AA-stacked regions form inside the QD [Fig. 4(d)], a stronger hybridization occurs, and therefore the energy increases. We note that in a pristine tBLG sheet, the states near the Dirac points also localize in the AA-stacked spots of the moiré pattern [62,68]. The semiclassical treatment of one-dimensional strained moiré in BLG [69] shows that the energies near the Dirac point are trapped in a *semiclassical potential* centered at the AA spots, and the electron localization is driven by this potential. Although the existence of such moiré potential wells in the AA regions of the tBLG structure has been discussed in Refs. [51,68,70], a systematic
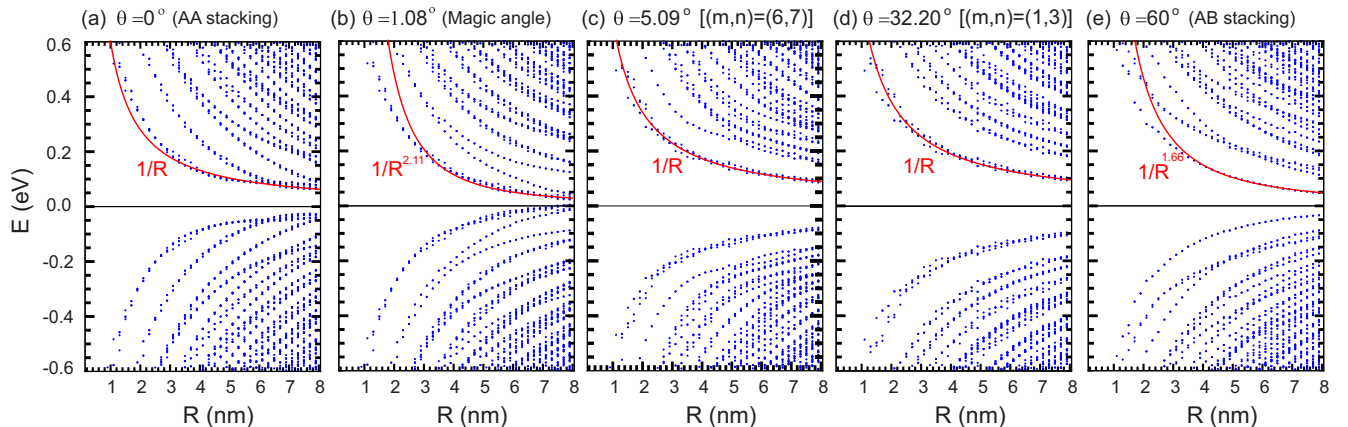
FIG. 5. Lowest-energy levels as a function of dot radius R for infinite-mass defined dot in the absence of a magnetic field. The results are plotted for five different twist angles: (a) $\theta = 0$ (AA stacking), (b) $\theta = 1.08°$ (magic angle), (c) $\theta_{6,7} = 5.09°$, (d) $\theta_{1,3} = 32.20°$, and (e) $\theta = 60°$ (AB stacking). In each case, the red solid curves show the power-law dependence $\sim \alpha R^{\beta}$ for the lowest electron energies up to $\epsilon \lesssim 0.17$ eV.
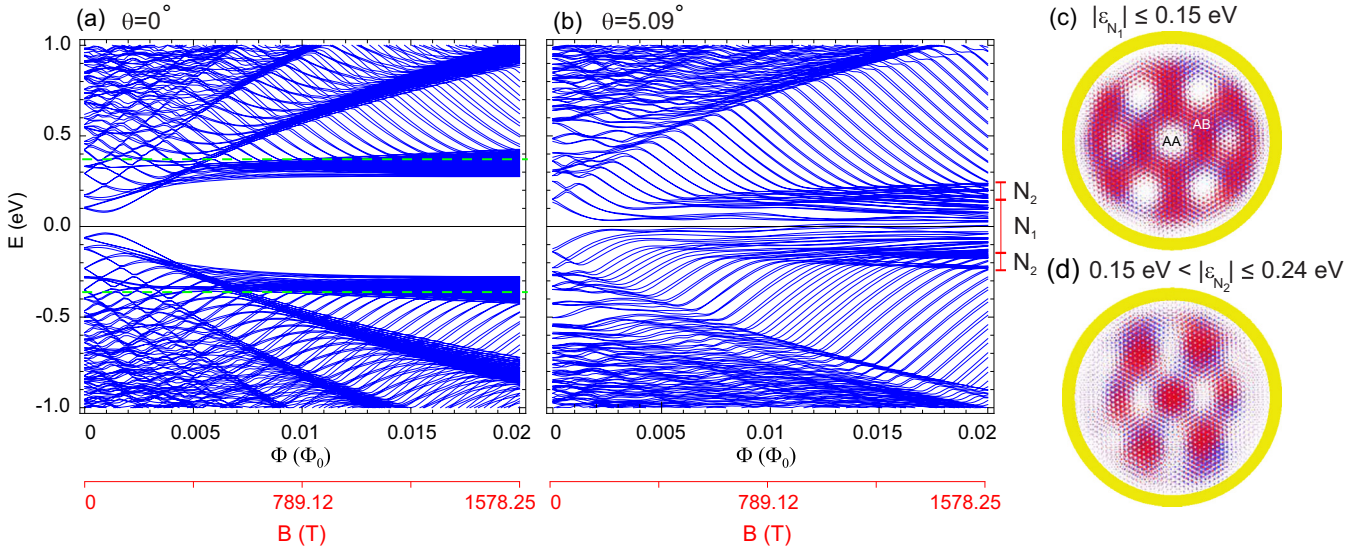
FIG. 6. (a), (b) Energy spectrum of a circular tBLG QD, of radius $R = 4.81$ nm, as a function of the magnetic flux Φ (in units of Φ_0) for (a) $\theta = 0$ and (b) a twist angle of $\theta_{6,7} = 5.09°$. The dashed green lines indicate the $\gamma_\pm = 0.37$ eV, which is the average interlayer coupling between the interacting adjacent atoms of two layers. (c),(d) Probability densities corresponding to the energy windows marked by N_1 and N_2 in panel (b) at $\Phi = 0.02\Phi_0$ ($B \approx 1578$ T, $l_B = 0.66$ nm $< L_{6,7} = 2.77$ nm). Layer 1 (2) is represented by the blue (red) color, and the yellow region indicates the mass potential barrier.

study (e.g., providing a semiclassical approach similar to the one in Ref. [69]) is needed to rigorously show this existence. On the other hand, for large twist angles, the period of the commensurate structure is too small to create well-defined AA- and AB-stacked regions and the system behaves as two decoupled monolayers [see Fig. 4(e) for $\theta = 32.20°$]. We have observed similar patterns for different QD sizes (including a dot with only a single moiré spot, i.e., $R = L_{m,n}$).

Figure 5 shows the energy levels as a function of the dot radius R for the five different twist angles (a) $\theta = 0°$ (AA-stacked BLG QD), (b) $\theta = 1.08°$ (magic angle), (c) $\theta_{6,7} = 5.09°$, (d) $\theta_{1,3} = 32.20°$, and (e) $\theta = 60°$ (AB-stacked BLG QD). The low-energy levels exhibit a power-law decay as functions of R and strongly depend on the twisting angle θ. The red solid curves show power-law fits (up to $\epsilon \lesssim 0.17$ eV) to the lowest-electron energy level. The AA- and AB-stacked QDs [Figs. 5(a) and 5(e)] exhibit an $\sim 1/R$ and $\sim 1/R^{1.66}$ dependence, respectively. These dependencies can be explained by the linear and quadratic low-energy dispersion in AA- and AB-stacked BLG sheets. A remarkable difference is seen at the magic twist angle $\theta = 1.08°$ [Fig. 5(b)], for which the energy gap between the electron and hole states closes rapidly when the dot radius increases. The lowest electron energy in this case shows an $\sim 1/R^{2.11}$ dependence. This behavior can be linked to the band flattening of the lowest moiré band at magic twist angles [53,54,71]. At $\theta_{1,3} = 32.20°$ we found that the interlayer coupling becomes extremely weak, the two layers are decoupled, and therefore the corresponding spectrum in Fig. 5(d) exhibits two copies of a monolayer graphene QD spectrum. This statement can also be confirmed through the localization of the charge density shown in Fig. 4(e) for $\theta_{1,3} = 32.20°$. Our fittings for the twisting angles $\theta_{6,7} = 5.09°$ and $\theta_{1,3} = 32.20°$ show an $\sim 1/R$ dependence.

V. LANDAU LEVELS

Here, we investigate the effect of a perpendicular magnetic field on the energy levels of tBLG QDs. As pointed out in Sec. IV, at large twist angles, a tBLG QD behaves as two decoupled monolayer QDs. Accordingly, we present our results for the small twist angle $\theta_{6,7} = 5.09°$ and compare with the case of an untwisted AA-stacked BLG QD ($\theta = 0$).

Figure 6 shows the magnetic levels, i.e., the so-called Fock-Darwin levels, of a circular tBLG QD with $R = 4.81$ nm, as functions of the magnetic flux threading one carbon hexagon Φ (in the units of Φ_0) for (a) $\theta = 0$ (untwisted) and (b) $\theta_{6,7} = 5.09°$. The Landau levels (LLs) in an AA-stacked BLG QD [$\theta = 0$, Fig. 6(a)] exhibit a band gap between the electron and hole levels for the whole range of magnetic field. As magnetic field increases, the discrete low-energy levels approach asymptotically the LLs of an AA-stacked BLG sheet for which the zeroth electron (hole) LLs are $\epsilon_\pm^{(0)} = \gamma_\pm \approx \pm 0.37$ eV, where $\gamma_\pm$ is the average interlayer coupling between the neighboring atoms (with cutoff $4a_{cc}$) [72]. Figure 6(b) shows the LLs of a tBLG QD with the twist angle $\theta_{6,7} = 5.09°$. A small twisting significantly affects the magnetic levels in tBLG QDs. As B increases, the energy gap closes and the lowest magnetic levels spread out between the electron and hole zeroth LLs of a pristine tBLG, which are different from those of AA- or AB-stacked BLG [73]. These are *edge* states, localized at the boundaries between the AA- and AB-stacked regions. Figure 6(c) shows the corresponding density distribution ρ_{N1} at $\Phi = 0.02\Phi_0$ ($l_B = \sqrt{\hbar/eB} = 0.66$ nm $< L_{6,7} = 2.77$ nm), where we summed over the energies with $|\epsilon_{N1}| \leqslant 0.15$ eV. For the energy range of 0.15 eV $< |\epsilon_{N2}| \leqslant 0.24$ eV, farther from ϵ_F, one can see that the carrier is mostly localized at the AA spots of the moiré pattern, Fig. 6(d). Approaching the tBLG LLs, as a result of
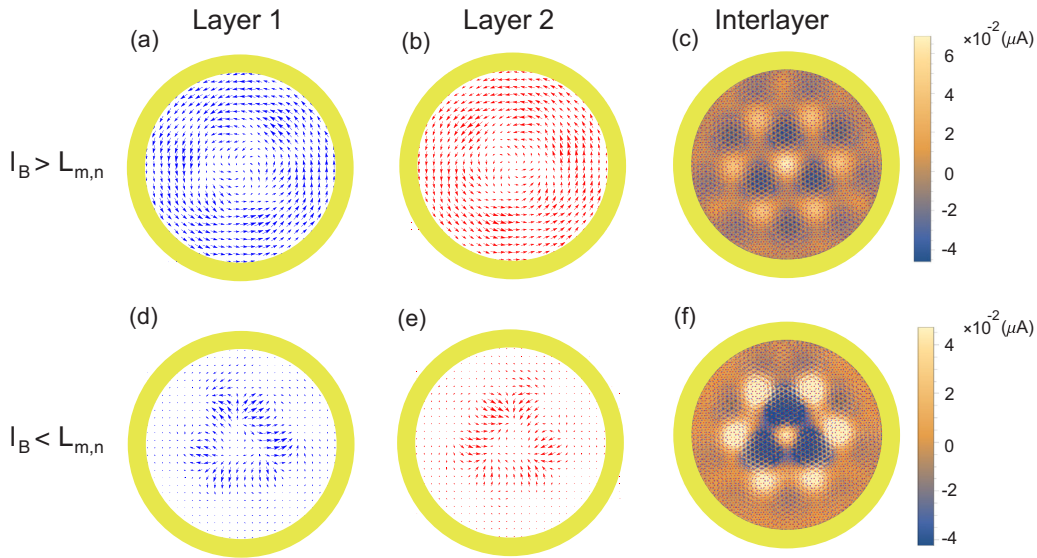
FIG. 7. Electron current density profile for a tBLG QD of radius $R = 4.81$ nm and with the twist angle of $\theta_{6,7} = 5.09°$ ($L_{6,7} = 2.77$ nm). The upper (lower) panel shows the result for $B = 40$ T ($B = 200$ T) for which $l_B = 4.06$ nm $> L_{6,7}$ ($l_B = 1.81$ nm $< L_{6,7}$). Panels (a), (d) and (b), (e), respectively, show the in-plane current vectors in layers 1 and 2, corresponding to the first two electron states shown in the energy spectrum of Fig. 6(b). (c), (f) Corresponding perpendicular interlayer current flowing between the dot layers. Light and dark regions, respectively, indicate the current directions out of and into the dot plane.

coupling between the moiré-lattice- and the magnetic-field-induced states, anticrossings appear in the spectrum.

Note that, at the low magnetic fields, for which the magnetic length l_B is greater than the moiré length $L_{m,n}$, the results (not shown here) are very similar to the case $B = 0$ (Sec. IV). We also note that, since we have considered the small sizes of the dots, the applied magnetic field in our calculations is too high to be achievable in experiments. However, in QDs, one can define a scaling factor and thus extend the results to lower B and larger QD sizes [74]. By setting the dot size R equal to the cyclotron radius at the Fermi energy, i.e., $R = l_B^2 k_F$, and using $E \approx \pm V_{pp\sigma}^0 \pm \hbar v_F k_F$ for the low-energy dispersion of the AA-stacked BLG, one can obtain k_F and consequently the scaling factor with respect to the magnetic field and size of the confinement area as $R = (E \pm V_{pp\sigma}^0)/(ev_F B)$. For the typical values of $E \pm V_{pp\sigma}^0 = 1$ eV, $v_F = 10^6$ m/s, and $B = 20$ T, we obtain $R = 50$ nm.

Finally, we consider the electron current of tBLG QD using Eqs. (9) and (10). The *in-plane* (*interlayer*) current at site i is defined as the sum of all outgoing current vectors from site i to other sites (to all sites in the other layer) [51]. In Fig. 7, we plot the current densities for a dot of radius $R = 4.81$ nm and the twist angle of $\theta_{6,7} = 5.09°$ ($L_{6,7} = 2.77$ nm). The results are shown for two different magnetic fields (upper panel) $\Phi = 0.0005\Phi_0$ ($B = 40$ T, $l_B = 4.06$ nm $> L_{6,7}$) and (lower panel) $\Phi = 0.0025\Phi_0$ ($B = 200$ T, $l_B = 1.81$ nm $< L_{6,7}$). Panels (a),(d) and (b),(e), respectively, show the in-plane current vectors in layers 1 and 2, summed over the first two electron states shown in the energy spectrum of Fig. 6(b). Corresponding interlayer currents are displayed in panels (c) and (f). As seen, irrespective of the ratio between l_B and $L_{m,n}$, the current densities are affected by the moiré pattern. In both cases, the interlayer current flows from layer 1 into layer 2

through the AA spots (light regions) and back through the AB spots (dark-blue regions). A similar effect was observed for other tBLG nanostructures [50,51]. As can be seen in Figs. 7(a) and 7(b), when $l_B > L_{m,n}$, the in-plane current components, with anticlockwise motion in both layers, flow toward the central AA spot in layer 1, and outward in layer 2. The central AA and its neighboring AB spots have the highest interlayer current density [Fig. 7(c)] and the lowest in-plane current density [Fig. 7(a,b)]. At a high magnetic field ($l_B < L_{m,n}$), one can obviously observe the increase of the interlayer current [cf. Figs. 7(c) and 7(f)]. On the other hand, the in-plane current components in each layer flow in opposite directions between the adjacent *source* and *sink* regions of the interlayer current; see Figs. 7(d) and 7(e).

VI. SUMMARY AND CONCLUDING REMARKS

In summary, using a tight-binding model we studied the electronic properties of circular QDs in twisted bilayer graphene defined by the infinite-mass boundary condition, and we investigated the effect of twisting angle on the energy levels and the corresponding density distributions in the absence and presence of a perpendicular magnetic field B. In the absence of a magnetic field, or when the magnetic length is greater than the moiré length ($l_B > L_{m,n}$), the low-energy levels are affected by the formation of a moiré pattern where the carriers confine at the AA-stacked regions. We found that, due to the hybridization between the mass-induced confinement and the AA-stacked localized states, the energy spectrum changes for small twist angles $\theta \lesssim 10°$. In the presence of a strong magnetic field where $l_B < L_{m,n}$, the energy gap of the untwisted QDs ($\theta = 0$) closes and the lowest LLs spread out over the gap, and they are associated with the edge states

localized at the boundaries between the AA- and AB-stacked regions.

Electron current investigation also showed that, irrespective of the ratio between the magnetic and moiré lengths, an applied perpendicular magnetic field causes interlayer charge flow between the dot layers, forming *source* and *sink* regions of the interlayer current at the AA and AB spots over the dot region. On the other hand, the in-plane current density profile exhibits a different pattern depending on the ratio between the magnetic and moiré length scales.

[1] Y. Cao, V. Fatemi, S. Fang, K. Watanabe, T. Taniguchi, E. Kaxiras, and P. Jarillo-Herrero, Nature (London) **556**, 43 (2018).

[2] Y. Cao, V. Fatemi, A. Demir, S. Fang, S. L. Tomarken, J. Y. Luo, J. D. Sanchez-Yamagishi, K. Watanabe, T. Taniguchi, E. Kaxiras, R. C. Ashoori, and P. Jarillo-Herrero, Nature (London) **556**, 80 (2018).

[3] M. Yankowitz, S. Chen, H. Polshyn, Y. Zhang, K. Watanabe, T. Taniguchi, D. Graf, A. F. Young, and C. R. Dean, Science **363**, 1059 (2019).

[4] A. V. Rozhkov, G. Giavaras, Y. P. Bliokh, V. Freilikher, and F. Nori, Phys. Rep. **503**, 77 (2011).

[5] A. D. Güçlü, P. Potasz, M. Korkusinski, P. Hawrylak, X. Li, S. P. Lau, L. Tang, R. Ji, and P. Yang, *Graphene Quantum Dots* (Springer, Berlin, 2014).

[6] D. Bischoff, A. Varlet, P. Simonet, M. Eich, H. C. Overweg, T. Ihn, and K. Ensslin, Appl. Phys. Rev. **2**, 31301 (2015).

[7] A. V. Rozhkov, A. O. Sboychakov, A. L. Rakhmanov, and F. Nori, Phys. Rep. **648**, 1 (2016).

[8] M. Wimmer, A. R. Akhmerov, and F. Guinea, Phys. Rev. B **82**, 045409 (2010).

[9] O. V. Yazyev, Rep. Prog. Phys. **73**, 056501 (2010).

[10] M. Ezawa, Phys. Rev. B **76**, 245415 (2007).

[11] J. M. Pereira, P. Vasilopoulos, and F. M. Peeters, Nano Lett. **7**, 946 (2007).

[12] J. H. Bardarson, M. Titov, and P. W. Brouwer, Phys. Rev. Lett. **102**, 226803 (2009).

[13] A. D. Güçlü, P. Potasz, and P. Hawrylak, Phys. Rev. B **84**, 035425 (2011).

[14] D. P. Zebrowski, E. Wach, and B. Szafran, Phys. Rev. B **88**, 165405 (2013).

[15] M. T. Allen, J. Martin, and A. Yacoby, Nat. Commun. **3**, 934 (2012).

[16] D. R. da Costa, M. Zarenia, A. Chaves, G. A. Farias, and F. M. Peeters, Carbon **78**, 392 (2014).

[17] A. M. Goossens, S. C. M. Driessen, T. A. Baart, K. Watanabe, T. Taniguchi, and L. M. K. Vandersypen, Nano Lett. **12**, 4656 (2012).

[18] D. Bischoff, M. Eich, O. Zilberberg, C. Rössler, T. Ihn, and K. Ensslin, Nano Lett. **15**, 6003 (2015).

[19] M. Mirzakhani, M. Zarenia, S. A. Ketabi, D. R. da Costa, and F. M. Peeters, Phys. Rev. B **93**, 165410 (2016).

[20] M. Mirzakhani, M. Zarenia, D. R. da Costa, S. A. Ketabi, and F. M. Peeters, Phys. Rev. B **94**, 165423 (2016).

[21] A. Kormányos, V. Zólyomi, N. D. Drummond, and Guido Burkard, Phys. Rev. X **4**, 011034 (2014).

[22] K. Lee, G. Kulkarni, and Z. H. Zhong, Nanoscale **8**, 7755 (2016).

[23] G. Luo, Z.-Z. Zhang, H.-O. Li, X.-X. Song, G.-W. Deng, G. Cao, M. Xiao, and G.-P. Guo, Front. Phys. **12**, 128502 (2017).

[24] Z. Lei, S. Xu, J. Wan, and P. Wu, Nanoscale **7**, 18902 (2015).

[25] B. Huo, B. Liu, T. Chen, L. Cui, G. Xu, M. Liu, and J. Liu, Langmuir **33**, 10673 (2017).

[26] P. Vishnoi, M. Mazumder, M. Barua, S. K. Pati, and C. N. R. Rao, Chem. Phys. Lett. **699**, 223 (2018).

[27] H. Abdelsalam, V. A. Saroka, and W. O. Younis, Physica E **107**, 105 (2019).

[28] B. Trauzettel, D. V. Bulaev, D. Loss, and G. Burkard, Nat. Phys. **3**, 192 (2007).

[29] C. L. Tang, W. H. Yan, Y. S. Zheng, G. S. Li, and L. P. Li, Nanotechnology **19**, 435401 (2008).

[30] Z. Z. Zhang, K. Chang, and F. M. Peeters, Phys. Rev. B **77**, 235411 (2008).

[31] P. Recher and B. Trauzettel, Nanotechnology **21**, 302001 (2010).

[32] J. Guttinger, T. Frey, C. Stampfer, T. Ihn, and K. Ensslin, Phys. Rev. Lett. **105**, 116801 (2010).

[33] G. Giavaras and F. Nori, Appl. Phys. Lett. **97**, 243106 (2010).

[34] M. Zarenia, A. Chaves, G. A. Farias, and F. M. Peeters, Phys. Rev. B **84**, 245403 (2011).

[35] M. Grüjić, M. Zarenia, A. Chaves, M. Tadić, G. A. Farias, and F. M. Peeters, Phys. Rev. B **84**, 205441 (2011).

[36] C.-J. Shih, A. Vijayaraghavan, R. Krishnan, R. Sharma, J.-H. Han, M.-H. Ham, Z. Jin, S. Lin, G. L. C. Paulus, N. F. Reuel, Q. H. Wang, D. Blankschtein, and M. S. Strano, Nat. Nanotechnol. **6**, 439 (2011).

[37] T. Ihn, J. Güttinger, F. Molitor, S. Schnez, E. Schurtenberger, A. Jacobsen, S. Hellmüller, T. Frey, S. Dröscher, C. Stampfer, and K. Ensslin, Mater. Today **13**, 44 (2012).

[38] M. Zarenia, B. Partoens, T. Chakraborty, and F. M. Peeters, Phys. Rev. B **88**, 245432 (2013).

[39] D. R. da Costa, M. Zarenia, A. Chaves, G. A. Farias, and F. M. Peeters, Phys. Rev. B **92**, 115437 (2015).

[40] G. Tsoukleri, J. Parthenios, C. Galiotis, and K. Papagelis, 2D Mater. **2**, 024009 (2015).

[41] D. R. da Costa, M. Zarenia, A. Chaves, G. A. Farias, and F. M. Peeters, Phys. Rev. B **93**, 085401 (2016).

[42] A. Belouad, Y. Zahidi, and A. Jellal, Mater. Res. Express. **3**, 055005 (2016).

[43] M. Mirzakhani, M. Zarenia, P. Vasilopoulos, and F. M. Peeters, Phys. Rev. B **95**, 155434 (2017).

[44] M. Eich, R. Pisoni, A. Pally, H. Overweg, A. Kurzmann, Y. Lee, P. Rickhaus, K. Watanabe, T. Taniguchi, K. Ensslin, and T. Ihn, Nano Lett. **18**, 5042 (2018).

[45] A. Tiutiunnyka, C. A. Duqueb, F. J. Caro-Loperac, M. E. Mora-Ramosa, and J. D. Correac, Physica E **112**, 36 (2019).

[46] E. Suárez Morell, R. Vergara, M. Pacheco, L. Brey, and L. Chico, Phys. Rev. B **89**, 205405 (2014).

[47] E. S. Morell, P. Vargas, P. Häberle, S. A. Hevia, and L. Chico, Phys. Rev. B **91**, 035441 (2015).

[48] M. Fleischmann, R. Gupta, D. Weckbecker, W. Landgraf, O. Pankratov, V. Meded, and S. Shallcross, Phys. Rev. B **97**, 205128 (2018).

[49] M. Pelc, E. S. Morell, L. Brey, and L. Chico, J. Phys. Chem. C **119**, 10076 (2015).

[50] D. Weckbecker, M. Fleischmann, R. Gupta, W. Landgraf, S. Leitherer, O. Pankratov, S. Sharma, V. Meded, and S. Shallcross, arXiv:1901.04712.

[51] W. Landgraf, S. Shallcross, K. Türschmann, D. Weckbecker, and O. Pankratov, Phys. Rev. B **87**, 075433 (2013).

[52] G. Giovannetti, P. A. Khomyakov, G. Brocks, P. J. Kelly, and J. van den Brink, Phys. Rev. B **76**, 073103 (2007); B. Sachs, T. O. Wehling, M. I. Katsnelson, and A. I. Lichtenstein, *ibid.* **84**, 195414 (2011).

[53] R. Bistritzer and A. MacDonald, Proc. Natl. Acad. Sci. USA **108**, 12233 (2011).

[54] J. M. B. Lopes dos Santos, N. M. R. Peres, and A. H. Castro Neto, Phys. Rev. B **86**, 155449 (2012).

[55] P. Moon and M. Koshino, Phys. Rev. B **87**, 205404 (2013).

[56] D. Weckbecker, S. Shallcross, M. Fleischmann, N. Ray, S. Sharma, and O. Pankratov, Phys. Rev. B **93**, 035452 (2016).

[57] E. J. Mele, Phys. Rev. B **81**, 161405(R) (2010).

[58] S. Shallcross, S. Sharma, and O. Pankratov, Phys. Rev. B **87**, 245403 (2013).

[59] A. V. Rozhkov, A. O. Sboychakov, A. L. Rakhmanov, and F. Nori, Phys. Rev. B **95**, 045119 (2017).

[60] P. R. Wallace, Phys. Rev. **71**, 622 (1947).

[61] J. C. Slater and G. F. Koster, Phys. Rev. **94**, 1498 (1954).

[62] G. Trambly de Laissardière, D. Mayou, and L. Magaud, Nano Lett. **10**, 804 (2010).

[63] M. Koshino and P. Moon, J. Phys. Soc. Jpn. **84**, 121001 (2015).

[64] T. Nakanishi and T. Ando, J. Phys. Soc. Jpn. **70**, 1647 (2001).

[65] S. Uryu, Phys. Rev. B **69**, 075402 (2004).

[66] R. Peierls, Z. Phys. **80**, 763 (1933).

[67] T. N. Todorov, J. Phys.: Condens. Matter **14**, 3049 (2002).

[68] G. Trambly de Laissardière, D. Mayou, and L. Magaud, Phys. Rev. B **86**, 125413 (2012).

[69] M. Vogl, O. Pankratov, and S. Shallcross, Phys. Rev. B **96**, 035442 (2017).

[70] P. San-Jose, J. González, and F. Guinea, Phys. Rev. Lett. **108**, 216802 (2012).

[71] S. Shallcross, S. Sharma, E. Kandelaki, and O. A. Pankratov, Phys. Rev. B **81**, 165105 (2010).

[72] It is worth mentioning that, as expected, at high magnetic fields, the energy levels converge to the AA-stacked BLG LLs. In several articles, e.g., Eq. (73) in Ref. [26], an analytical formula for the LLs of AA-stacked BLG was obtained, for which only the nearest-neighbor interlayer hopping was taken into account. Here, because we set the cutoff of $4a_{cc}$ for the interlayer coupling, the formation of the LLs, in the case of the AA-stacked dots, does not coincide with those obtained from the mentioned formula. However, qualitatively, they follow the LLs predicted by that equation.

[73] R. de Gail, M. O. Goerbig, F. Guinea, G. Montambaux, and A. H. Castro Neto, Phys. Rev. B **84**, 045436 (2011).

[74] D. K. Ferry, L. Huang, R. Yang, Y. C. Lai, and R. Akis, J. Phys.: Conf. Ser. **220**, 012015 (2010).